Air Force Institute of Technology

AFIT Scholar

5-3-2022

Particle-in-cell Simulations of Ion Dynamics in a Pinched-beam Diode

Jesse C. Foster
Air Force Institute of Technology

John W. McClory
Air Force Institute of Technology

S. B. B. Swanekamp
U.S. Naval Research Laboratory

D. D. Hinshelwood
U.S. Naval Research Laboratory

A. S. Richardson
U.S. Naval Research Laboratory

See next page for additional authors

Recommended Citation

J. C. Foster, J. W. McClory, S. B. Swanekamp, D. D. Hinshelwood, A. S. Richardson, P. E. Adamson, J. W. Schumer, R. W. James, P. F. Ottinger, D. Mosher; Particle-in-cell simulations of ion dynamics in a pinched-beam diode. Physics of Plasmas 1 May 2022; 29 (5): 053103. https://doi.org/10.1063/5.0089904

Authors

Jesse C. Foster, John W. McClory, S. B. B. Swanekamp, D. D. Hinshelwood, A. S. Richardson, Paul E. Adamson, J. W. Schumer, R. W. James, P. F. Ottinger, and D. Mosher

Particle-in-cell simulations of ion dynamics in a pinched-beam diode ⊘

J. C. Foster ✉ ⓘ ; J. W. McClory ⓘ ; S. B. Swanekamp ⓘ ; D. D. Hinshelwood ⓘ ; A. S. Richardson ⓘ ;
P. E. Adamson ⓘ ; J. W. Schumer ⓘ ; R. W. James ⓘ ; P. F. Ottinger ⓘ ; D. Mosher

Check for updates

View Online   Export Citation   CrossMark

Particle-in-cell simulations of ion dynamics in a pinched-beam diode

View Online   Export Citation   CrossMark

J. C. Foster,[1,a] [iD] J. W. McClory,[1] [iD] S. B. Swanekamp,[2] [iD] D. D. Hinshelwood,[2] [iD] A. S. Richardson,[2] [iD]
P. E. Adamson,[2] [iD] J. W. Schumer,[2] [iD] R. W. James,[3] [iD] P. F. Ottinger,[4] [iD] and D. Mosher[4]

AFFILIATIONS

[1] Air Force Institute of Technology, Dayton, Ohio 45433, USA
[2] U.S. Naval Research Laboratory, Washington, DC 20375, USA
[3] U.S. Coast Guard Academy, New London, Connecticut 06320, USA
[4] Syntek Technologies, Fairfax, Virginia 22031, USA

[a] Author to whom correspondence should be addressed: Jesse.Foster@afit.edu

ABSTRACT

Particle-in-cell simulations of a 1.6 MV, 800 kA, and 50 ns pinched-beam diode have been completed with emphasis placed on the quality of the ion beams produced. Simulations show the formation of multiple regions in the electron beam flow characterized by locally high charge and current density ("hot spots"). As ions flow through the electron-space-charge cloud, these hot spots electrostatically attract ions to produce a non-uniform ion current distribution. The length of the cavity extending beyond the anode-to-cathode gap (i.e., behind the cathode tip) influences both the number and amplitude of hot spots. A longer cavity length increases the number of hot spots yet significantly reduces the amplitude producing a smoother, more uniform ion beam than for shorter cavities. The net current and the ion bending angles are also significantly smaller with long cavities.

Published under an exclusive license by AIP Publishing. https://doi.org/10.1063/5.0089904

I. INTRODUCTION

Much of the early work on the properties of intense ion beams was guided by the inertial confinement fusion (ICF) community.[1–3] Significant efforts within the ICF community were driven by the discovery of intense ion beams produced in pinched electron-beam diodes (PBDs).[4,5] Some of these efforts studied a wide range of ion-beam properties using experiments, theory, and/or simulations.[6–11] It was found that the ion-beam micro-divergence (the standard deviation cone about an inward ion-bending angle) is a key limiting factor for focusing the beam onto an ICF target.[12] That realization led to a decade-long investment in developing the applied-B diode as a low micro-divergence light ion-beam source.[13–15] As part of this development, extensive three-dimensional (3D) particle-in-cell (PIC) simulations were instrumental in identifying instabilities in the charged-particle flow as the main source of micro-divergence in the applied-B diode.[13–15] Beyond ICF, PBDs are important sources of x-rays for flash radiography.[16,17] Even though x-ray production is mainly driven by electron dynamics, the physics that affect the ion-beam properties in the PBD has not received recent attention involving PBD simulation.[18] There is, however, a renewed interest in intense ion

beams for material science applications.[19,20] These applications require ion beams with uniform fluences over large areas. This paper presents new PIC results that focus on the role charged-particle dynamics in the diode play on the quality of the ion beam; the role of electrode-plasma dynamics will be discussed in future work, as will the discussion and analysis of micro-divergence as it relates to ion-beam quality.

A PBD consists of an annular cathode that emits electrons, which are accelerated toward a planar anode. Once electrons deposit energy on an area of the anode to exceed the threshold for thermal desorption of impurities from the surface, a plasma forms there, producing a zero-work function surface from which ions can be drawn into the anode–cathode (AK) gap. The presence of ion space-charge reduces the local electric field near the anode and allows the electron flow to bend strongly (i.e., pinch) toward the axis as a result of the magnetic field.[21,22] As the electron beam pinches to the axis, the whole anode surface is heated and begins to emit ions. This two-dimensional (2D) process provides the high ion current fraction in the PBD.[4,5] The average electric field, which is given in units of electric potential per length V/d, remains the same for any given voltage. If there is no ion emission (e.g., insufficient heating), the ion charge remains on the surface of the

anode and the electric field acts to pull electrons to the anode before the magnetic field can pinch the electron flow. To achieve a strong pinch, a significant ion space charge must exist in the AK gap, which is defined as the axial region between the anode foil and the cathode tip. Because protons are the desired ion-beam component, a polyethylene anode with a high proton fraction is used in experiments.[23] Previous measurements with a polyethylene anode show that the ion beams are highly non-uniform with spotty structure.[24] From these measurements, a micro-divergence of 150–200 mrad is estimated.

We investigate two possible sources of non-uniformity in the PBD: (1) beam azimuthal filamentation possibly due to instabilities and non-uniformity of the electrode plasmas and (2) the radial distribution and evolution of the charged particle flows in the diode. Instabilities in the cathode plasma have been investigated as a source of azimuthal filamentation of the electron beam.[25] The azimuthal filamentation of the electron beam combined with the radial distribution of the charged particle flow in the AK gap could produce spotty ion emission. Additionally, experiments have shown that the anode and cathode plasmas expand into the AK gap producing impedance collapse as the effective AK gap closes.[26] Simulations of the cathode plasma have not been done; however, simulations of the anode plasma show that the plasma distorts the diode equipotential surfaces so that the surface of the anode plasma is effectively at the same potential as the anode.[27,28] None of these simulations show evidence of plasma instabilities. However, it is not clear whether the simulations are sufficiently resolved to model accurately the short wavelength instabilities that could lead to filamented or spotty ion emission.

Section II provides details of how the simulations were setup and modeled. Next, Sec. III illustrates and defines electron hot spots. We discuss the physics of their formation and how their presence affects ion current densities. Then, Sec. IV explores how hot spots and their effects on ion current densities vary due to cavity length. Finally, Sec. V investigates ion bending angles and how they vary by cavity length.

II. SIMULATION SETUP

We obtain simulation results using the finite-difference time-domain PIC code, CHICAGO.[29,30] All simulations have a 2D cylindrical R–Z geometry as shown in Fig. 1(a). In general, electron beam emission comes from a thin annular cathode tip with an outer radius of 6 cm and a thickness of 3 mm. The anode is a 13-μm-thick polyethylene foil placed 5 mm from the cathode tip. Power is supplied to the diode using a 8.5-cm-long cylindrical transmission line with an inner radius of 10 cm and an outer radius of 15 cm. Figure 1(b) is a 3D rendering of the simulation geometry in CHICAGO.

The length of the cavity behind the front face of the cathode tip is defined by the placement of the Kimfol, the surface through which the ion beam is extracted.[31] Kimfol is a thin poly-carbonate that separates a region in which ions are generated and another region in which ions are transported to a target. The foil is thin enough to sustain small pressure differences, yet thin enough to readily allow the ion beam to pass through relatively unaffected. The location of the Kimfol and its relative placement behind the cathode tip determines the source of neutralizing electron charge and the region from which current flows as the ion beam leaves the AK gap region and moves through the cavity.[32] When the Kimfol is located flush or slightly behind the cathode tip, neutralizing electron flow comes primarily from the Kimfol surface. When the Kimfol is a few AK gaps [1 AK gap = 5 mm; see Fig. 1(a)] behind the cathode tip, ions exit the AK gap and may pull from the pinched stream of electrons that are emitted from the cathode tip.

Electron emission occurs from the surfaces of the Kimfol and from the face as well as the inner and outer surfaces of the cathode tip. These surfaces are highlighted light blue in Fig. 1. Electrons emitted
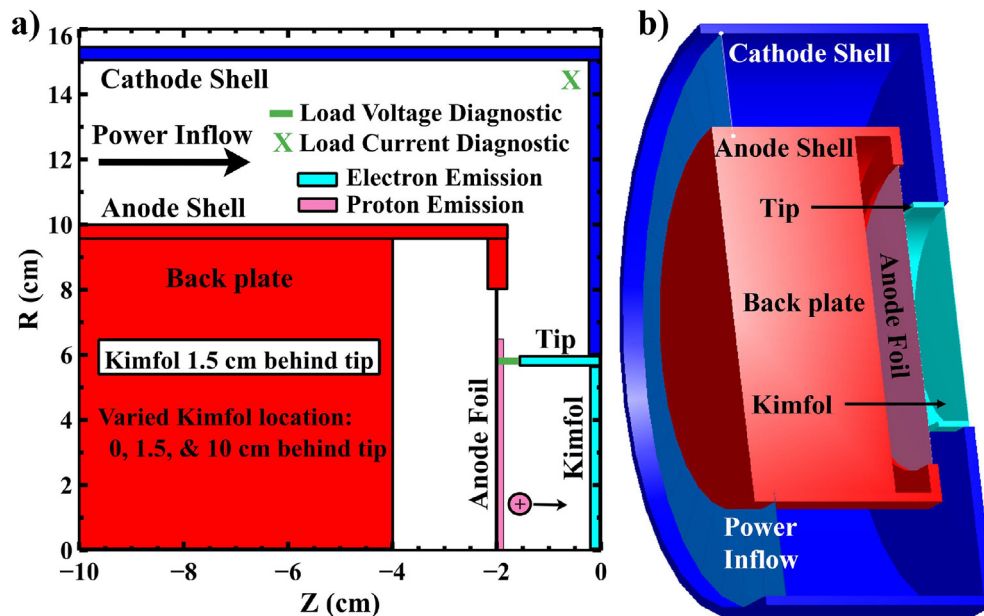

FIG. 1. (a) 2D R–Z PIC simulation geometry. Power is supplied at the inflow boundary ($Z = -10$ cm). Electron emission is enabled from the light blue area; and proton emission is enabled from the pink area. (b) A 3D rendering of this geometry in CHICAGO.

from each of these surfaces are a separate species in the simulation so that their contribution to overall charge and current neutralization can be tracked. Electron emission is enabled once the electric field locally exceeds 200 kV/cm on the surface.[33,34] Once the threshold electric field is exceeded, enough charge is emitted into the vacuum region to drive the electric field perpendicular to the surface to zero at that location. This is referred to as space-charge limited (SCL) emission and results in electron flow from the cathode to the anode.[35–38]

Proton emission is enabled from the surface of the anode foil highlighted in pink in Fig. 1. The generally accepted mechanism for ion emission from a metallic anode is that ions are drawn from a zero-work function plasma that forms from material that is out-gassed and then ionized.[39,40] This happens once the electron beam has deposited enough energy on the anode surface to break the bonds that weakly bind contaminants to the surface. For most of the metallic surfaces used in pulsed-power devices, the binding energy is a fraction of an eV so that significant outgassing does not occur until the surface temperature exceeds 700 °K. However, these simulations use a polyethylene anode, which melts at 420 °K. In this case, a zero-work function plasma is assumed to be created from the vapor pressure that forms above the melted anode surface once the surface temperature exceeds 420 °K. For polyethylene, only proton emission is allowed because of the large mass difference between carbon and hydrogen.

Regarding the anode, it is necessary to point out that, experimentally, the polyethylene foil is 13 μm thick, which requires a higher resolution than the simulations. The thickness of the foil in the simulation geometry is made to be 200 μm thick to ensure the foil width is adequately represented by containing a reasonable number of grid cells. To simulate a 13-μm foil, the density is adjusted by a factor of 13/200 when generating the electron scattering cross sections for the simulation. Any transverse electron displacement error caused by this adjustment is small and is reduced as electron reflexing back and forth through the anode foil is highest early in the pulse and subsides later in the pulse. It subsides due to the electron flow being strongly pinched by the magnetic field so that electrons flow radially inward inside the vacuum AK gap until reaching the axis at $R = 0$ cm.

An external circuit that consists of a driving voltage, $V_s(t)$, in Eq. (1) and a series resistance is used to drive power into the simulations. The series resistance is set to $R_s = 3 \, \Omega$, and the driving or applied voltage is taken to be

$$V_s(t) = V_o \sin^2\left(\frac{\pi t}{2\tau}\right) \tag{1}$$

in which $V_o = 4$ MV is the open circuit voltage and $\tau = 50$ ns is the rise time. This voltage is converted to a radial electric field with a 1/R profile that is used to drive a transverse electromagnetic wave down the cylindrical transmission line. With these choices for the driving circuit, the peak diode voltage and current with a load impedance of $Z_L = 2 \, \Omega$ are $V_L = 1.6$ MV and $I_L = 800$ kA, respectively.

Typical voltage and current traces from the simulations are shown in Fig. 2. The simulations are terminated at peak power ($t = 50$ ns). Figure 2(a) shows the input (red curve) and load (blue curve) voltage time histories in the simulations. The difference between the two voltages is the inductive drop between the drive port and the diode load when current starts to flow. The drop in the load voltage at approximately 25 ns (i.e., near the center of the figure) is attributed to ion turn-on that produces a rapid change in the diode impedance as the diode transitions from single-species electron flow to strongly pinched electron and ion flow. Figure 2(b) is a representative simulation current history. It shows the total-, electron-, and ion-current for a diode where the Kimfol is placed 1.5 cm behind the cathode tip as the blue, green, and purple curves, respectively. Current histories for the other cavity lengths in this study appear similar. At 50 ns, the ion current is 400 kA, which accounts for ~50% of the total, and which agrees well with experimentally measured and theoretically predicted ion currents.[8,41,42]

Special attention is applied to the computational grid. A higher grid resolution is needed near the axis because the electron beam compresses into a small area as it pinches. Electron densities exceed 10^{15} cm^{-3} in the simulations. Since experiments do not measure a current density as high as simulations near the axis, the electrons were given an initial temperature of 10 keV as they leave the cathode. This
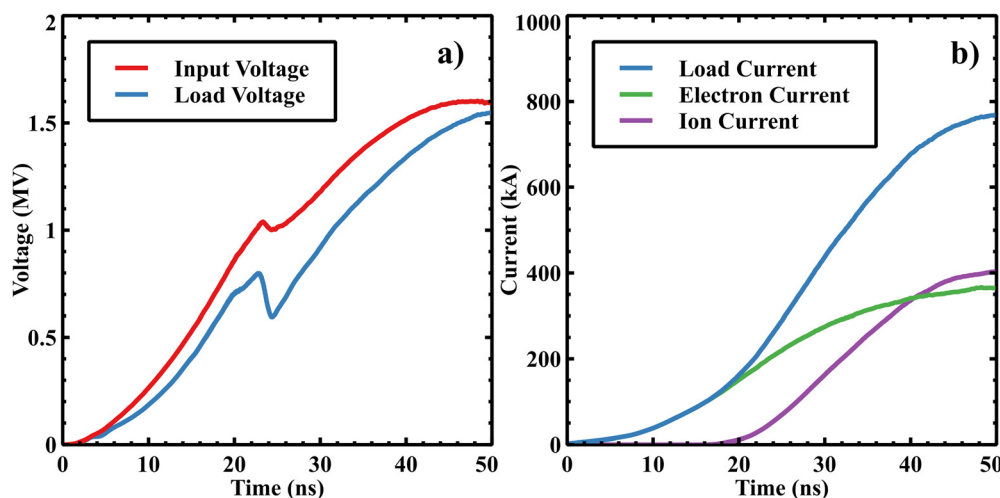

FIG. 2. Representative diode voltage and current histories for a 50 ns pulse. (a) Input and load voltage histories. (b) Load, electron, and ion current histories.

initial temperature gives the electrons some angular momentum that keeps a portion of the beam from reaching the axis. Instead of a highly focused beam near $R = 0$ cm, the large initial temperature causes the electrons in the pinch to spread out between $R = 0$ and 1 cm as they connect with the anode. This artificially high temperature is intended to model the electron emission from non-uniform or unstable plasmas. While the behavior of the electron beam near $R = 0$ cm depends on the initial temperature, the simulation results away from $R = 0$ cm are relatively unchanged.

As the electron beam pinches, it also creates a virtual cathode where the magnitude of the electric field is small. For the PBD, the virtual cathode position is shown as the white contour in Fig. 3(a). It appears on the left-hand side and at the bottom of the figure. As seen in this figure, the position of the virtual cathode is compressed closer to the anode as the electron beam pinches. This makes the effective gap near the axis much smaller than the physical AK gap. Because of this, a small radial electric field exists that imparts a small inward velocity to the ions as they are accelerated from the anode to the virtual cathode. This amounts to a small inward ion "bending angle" as will be discussed below in Sec. V. However, symmetry demands that this radial electric field and its resulting bending angle must vanish at the axis. Resolving the rapidly spatially varying fields and the high-particle densities required a grid resolution of 25 μm near $R = 0$ cm for all simulations.

Finally, the electron plasma frequency, ω_p, and the electron cyclotron frequency, ω_c, were monitored to maintain stability and accuracy. As such, the time step, Δt, for the simulations was chosen to keep $\omega_p \Delta t$ and $\omega_c \Delta t$ on the order of 0.1. This required a Courant number of 0.2 and 0.4 for smaller and larger cavity simulations, respectively.

III. ELECTRON HOT SPOTS

Simulations were performed that placed the Kimfol 0, 1.5, and 10 cm behind the cathode tip. Figure 3(a) shows current-enclosed contours, $2\pi r B_\theta / \mu_0$, in units of kA, and Fig. 3(b) shows linear electron

current density, $2\pi r |J_e|$, in units of MA/cm, both at 50 ns for Kimfol placed 1.5 cm behind the cathode tip.

In Fig. 3(a), current flows parallel to the black contour lines and the amount of current that flows is determined by the difference between contour levels. For all of the current enclosed plots shown in this paper, the difference between contour levels is 100 kA. Regions of space in which the contours are closely spaced correspond to regions of high current density and vice versa. Figure 3(b) shows hot spots of higher electron current density in red. These hot spots correspond to the convergence of the contours in Fig. 3(a). In the absence of ion current, the contours are the integral of the electron current density. Thus, electron current density is higher where the contours are concentrated.

Electrons emitted from the outer radius of the cathode tip are born in a strong magnetic field. This causes the electron orbits to be bent mostly away from the anode and flow radially inward. Electrons emitted from the inner radius of the cathode tip are born in a weaker (factor of 2 lower) magnetic field and are accelerated toward the anode by a strong electric field. When these two streams cross, a region of high charge and current density is created. This region is referred to as a "hot spot" in the electron flow. As the electrons from the outer radius continue beyond the first hot spot, the magnetic field weakens but the strong electric field causes electrons to decelerate. Eventually, the axial speed of the electrons reaches zero (even though their angular velocity is non-zero). This position at which this occurs is the virtual cathode. As the electrons born on the inner radius of the cathode tip continue beyond the first hot spot, they experience a large magnetic field and their orbits are bent away from the anode. These two streams cross again to form a second hot spot. This crossing process continues and additional hot spots are formed as the electrons $\vec{E} \times \vec{B}$ drift radially inward. These hot spots are shown by the peaks in Fig. 4 that shows a radial lineout of the linear electron current density at a point 2 mm off the anode surface.

The presence of these hot spots has a profound effect on the linear ion current density. The associated large electron charge density creates a locally large space-charge electric field that modulates the linear ion-beam current density as it passes through the electron space-charge cloud. Figure 5 shows the contours of the magnitude of the
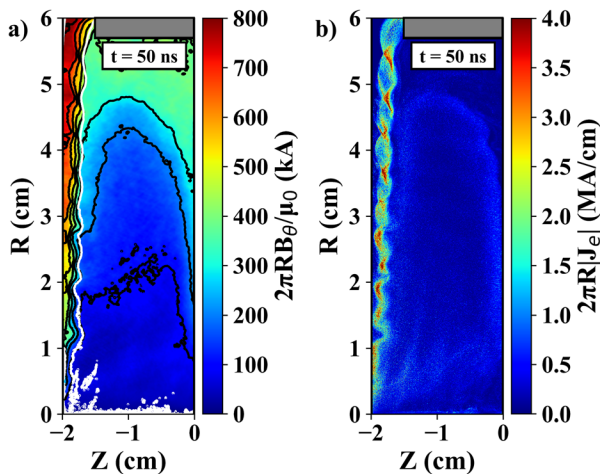

FIG. 3. Kimfol placed 1.5 cm behind cathode tip at 50 ns. (a) Current enclosed contours where current flows parallel to black lines separated by ~100 kA. Also shown is a white contour that shows the approximate position of the virtual cathode. (b) Linear electron current density with hot spots shown in red.
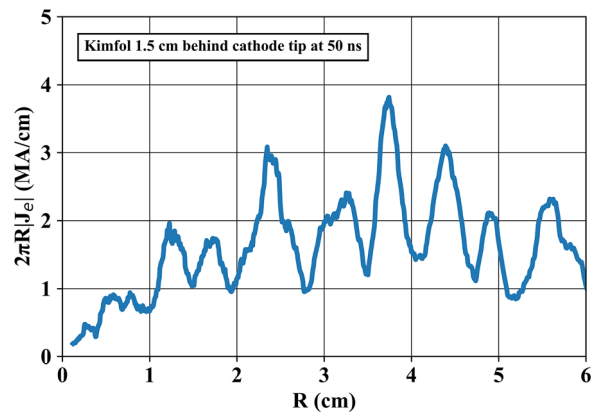

FIG. 4. Kimfol placed 1.5 cm behind cathode tip at 50 ns. Linear electron current density radial lineout at a point 2 mm off the anode surface. The peaks coincide with hot spots in Fig. 3.
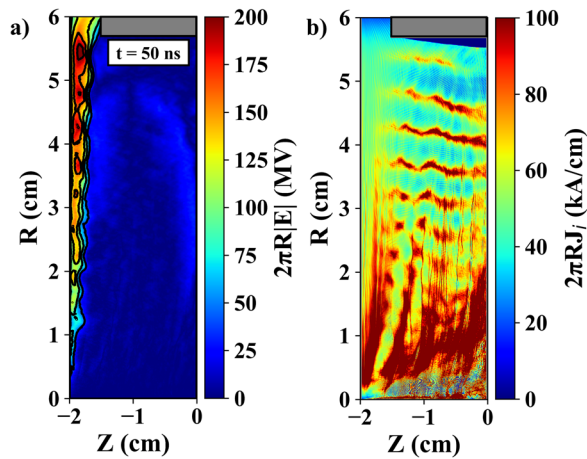
FIG. 5. Kimfol placed 1.5 cm behind cathode tip at 50 ns. (a) Linear electric field contour plot. (b) Linear ion current density.

FIG. 7. Kimfol placed flush to the cathode tip at 50 ns. (a) Current-enclosed contour plot where current flows parallel to black lines that are separated by ∼100 kA. (b) Linear electron current density with hot spots shown in red.

electric field [Fig. 5(a)] and the linear ion current density [Fig. 5(b)]. Regions of high linear electric field due to the hot spots are shown by the red structures in the upper-left portion of the plot in Fig. 5(a). These regions correspond to high linear ion current density also shown in red in Fig. 5(b).

Figure 6 shows lineouts of the linear ion current density at a point 2 mm off the anode and Kimfol. The linear ion current density near the Kimfol show peaks in orange that correspond to the streaks of red in Fig. 5(b). Note that all plots of J_e, J_i, and $|E|$ in this paper are multiplied by $2\pi R$. This provides visual clarity (e.g., the integral of either curve in Fig. 6 gives the ion current).

Figure 6 illustrates that ion flow is greatly modified between the anode and Kimfol. Ion emission is smooth along the anode (blue line); however, the linear ion current density is distorted by the hot spots as ions move through the electron space-charge cloud that result in peaks in the linear ion current density at the Kimfol (orange line). The large linear current densities for R < 1 cm in Fig. 6 are due to high number densities near the axis where the electron beam pinches and the
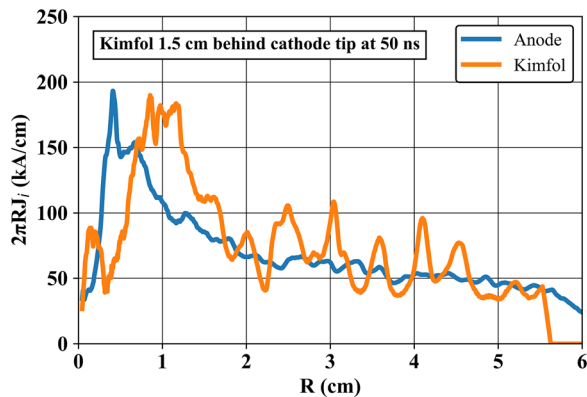
electron flow connects to the anode. This enhances the ion-beam current from this region of the anode. Outside this region, the oscillations caused by the electron hot spots results in about a factor of two modulation in the ion current.

IV. HOT SPOT VARIATION WITH KIMFOL PLACEMENT

Our results indicate that electron hot spots form regardless of Kimfol location behind the cathode tip. This is illustrated in Figs. 7 and 8 that show the current-enclosed contours and the linear electron current density for cases where the cavity length is 0 and 10 cm, respectively. Hot spots are seen in these two scenarios as indicated by a convergence of the current-enclosed contours, Figs. 7(a) and 8(a), which correspond to the regions of high linear electron current density indicated in red in Figs. 7(b) and 8(b).

FIG. 6. Kimfol placed 1.5 cm behind the cathode tip at 50 ns. Linear ion current density along a radial lineout 2 mm off the anode surface (blue) and the back of the cavity (i.e., the Kimfol surface) (orange).
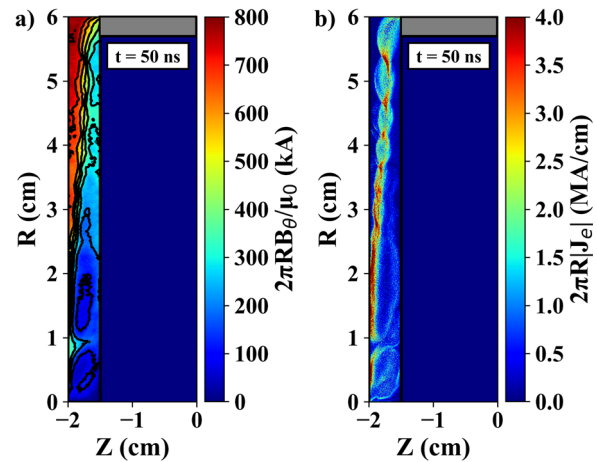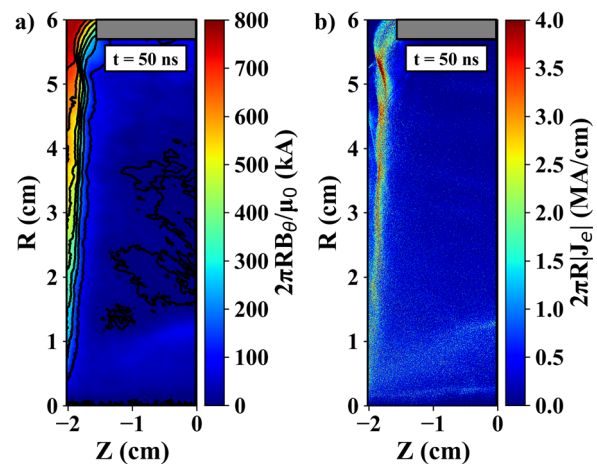

FIG. 8. Kimfol placed 10 cm behind the cathode tip at 50 ns. (a) Current-enclosed contour plot where current flows parallel to black lines that are separated by ∼100 kA. (b) Linear electron current density with hot spots shown in red.

When the cavity length is zero, there is a reduction in the number of hot spots between $R = 1$ and 3 cm, as shown in Fig. 7. The electron pinch in Fig. 7(a) is compressed close to the anode foil and the current-enclosed contours do not converge in that region. This electron pinch compression and subsequent reduction in number of hot spots is reflected in Fig. 7(b) in which there are fewer pockets of red where the linear electron current density is less dense in those regions.

The blue curve in Fig. 9 shows a lineout of the linear electron current density at a point 2 mm off the anode surface ($Z = -1.8$ cm). This plot quantitatively shows the amplitude of the linear electron current density is reduced between $R = 1$ and 3 cm. The Kimfol placement compresses the electron pinch due to the presence of neutralizing electrons emanating from the Kimfol surface. This causes the electron pinch to connect to the anode at a higher radial location prior to reaching the axis at $R = 0$ cm.

Figure 8(b) shows the linear electron current density for the case where the cavity length is 10 cm. It shows fewer pockets of red as compared to Figs. 3(b) and 7(b). Additionally, the current-enclosed contours for the case, in which the cavity length is 10 cm [Fig. 8(a)], are not as tightly spaced as they are for shorter cavities. The spacing of the contours indicates a reduction in number and amplitude of hot spots. The orange curve in Fig. 9 is a lineout of the linear electron current density in the AK gap at a point 2 mm from the anode surface. For radii between $R = 0$ and 5 cm, the frequency of hot spot occurrence increased, but the corresponding amplitudes are substantially smaller compared to the blue curve in Fig. 4 where the Kimfol was placed 1.5 cm behind the tip. From this, we conclude that lengthening the cavity smooths out hot spots.

While electron hot spots exist in all of the simulation results shown in this paper, the effect on the radial profile of the ion beam at the Kimfol surface in the back of the cavity is different. Figure 10(a) shows the linear electric field, and Fig. 10(b) shows the linear ion current density in the diode gap; Fig. 11 shows the corresponding lineouts of the linear ion current density along the anode and Kimfol for the case where the cavity is flush with the cathode tip face.

The blue line in Fig. 11 shows moderate peaks for $R < 1$ cm and a large peak at approximately $R = 2.25$ cm along the anode surface. This large peak is where the majority of the electron flow connects with the
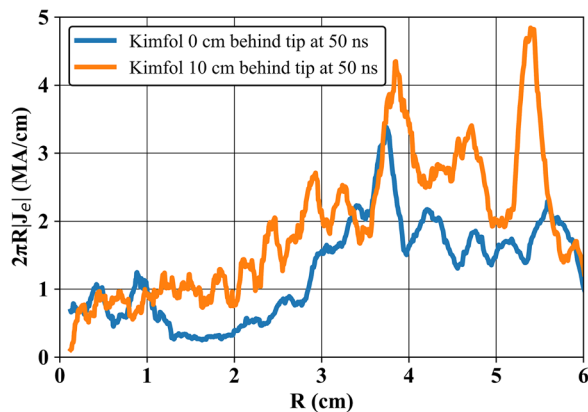

FIG. 10. Kimfol placed flush with the cathode tip at 50 ns. (a) Linear electric field contour plot. (b) Linear ion current density.

anode. It appears in Fig. 10(b) that the linear ion current density reflects the high concentration of electrons in the electron pinch from approximately $R = 2$ to 4 cm.

The orange line in Fig. 11 shows that there are large peaks for $R < 2$ cm and nearly constant, but significantly lower, linear ion current density for $R > 2$ cm near the Kimfol. For $R > 2$ cm, small peaks are shown that are caused by electron hot spots. This is similar to Fig. 6, which shows the linear ion current density near the anode and Kimfol when the Kimfol is 1.5 cm behind the tip. However the amplitude of the peaks is small. In Fig. 11, the distance between the anode and Kimfol is small, which causes the linear ion current density peaks beyond the electron hot spots to be small. This result shows that hot spots have less of an effect on the linear ion current density profile at the Kimfol surface when the Kimfol is flush with the cathode tip as compared to when the Kimfol is placed at a location 1.5 cm behind the cathode tip.

Figure 12 shows the linear electric field contours [Fig. 12(a)] and linear ion current density [Fig. 12(b)] in the diode gap when the cavity length is 10 cm. The linear electric field contours are smoother and the

FIG. 9. Linear electron current density at 50 ns measured 2 mm off the anode in the AK gap for two scenarios: (1) Kimfol placed flush to cathode tip (blue) and (2) Kimfol placed 10 cm behind the cathode tip (orange).
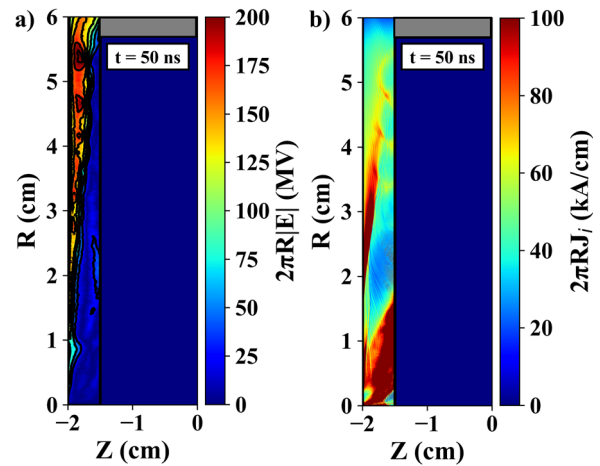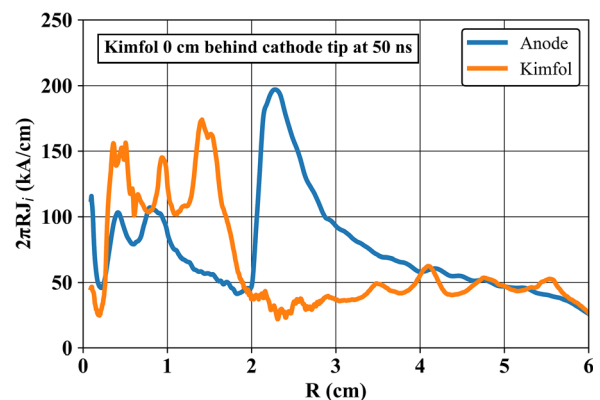

FIG. 11. Kimfol flush with cathode tip at 50 ns. Linear ion current density at a point 2 mm off the anode (blue) and Kimfol (orange).
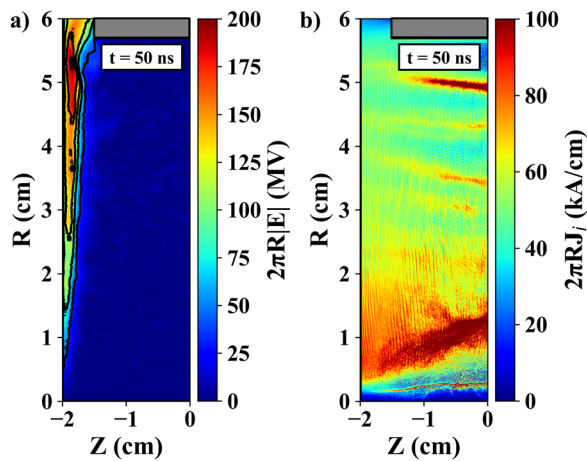
FIG. 12. Kimfol placed 10 cm behind cathode tip at 50 ns. (a) Linear electric field contour plot. (b) Linear ion current density. Note (a) and (b) encompass only the region 2 cm off anode surface.

hot spot effects on the linear ion current density appear reduced as compared to the two smaller cavity cases in Figs. 5 and 10.

Figure 13 compares the linear ion current density at the same location off the anode surface at $Z = 0$ cm in Figs. 5 and 12. This location is 2 cm off the anode surface for both a large cavity (Kimfol 10 cm behind the tip) and a smaller cavity (Kimfol 1.5 cm behind the tip). Note that 2 cm off the anode surface for the smaller cavity case is at the Kimfol surface. The region between $R = 1.5$ and 5 cm in Fig. 13 confirms that hot spot effects are reduced or washed out for larger cavities.

The lineout of the linear ion current density 2 mm off the anode and at the back surface of the cavity when the cavity length is 10 cm is shown in Fig. 14. The blue line shows a linear ion current density that is smooth along the anode surface and varies by $\sim$25 kA/cm from $R = 0.5$ to 5.5 cm. This roughly uniform profile away from the axis agrees reasonably well with previous PBD experiments.[8] However, the orange line shows a linear ion current density profile at the Kimfol with numerous peaks near $R = 3$ cm. Also, the linear ion current
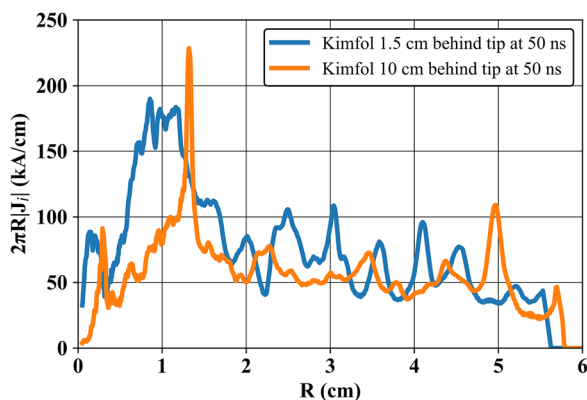

FIG. 13. Linear ion current density lineout as measured 2 cm off anode surface for a large (orange) and smaller (blue) cavity at 50 ns.
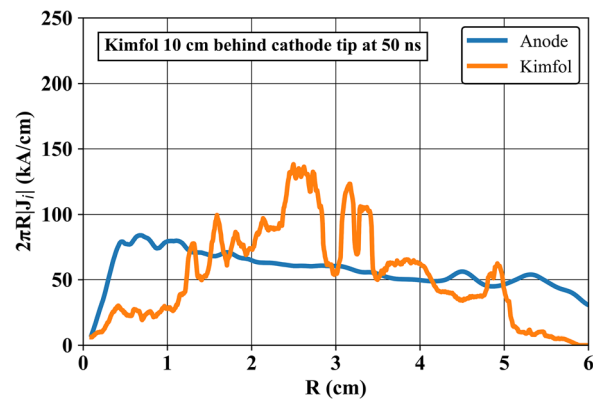

FIG. 14. Linear ion current density lineout as measured at a point 2 mm off the anode (blue) and at the back of the 10-cm-long cavity (orange) at 50 ns. Electron emission temperature is 10 keV.

density values for $R < 1$ cm and $R > 5$ cm are reduced substantially below the anode values at those same locations. Thus, in Fig. 14, the effect of hot spots on the linear ion current density at the Kimfol is not as pronounced as compared to the other two scenarios where the linear ion current density peaks correspond to electron hot spot locations.

The orange line in Fig. 14 requires explanation, and Fig. 15 provides the required insight. It shows the linear ion current density for the 10-cm-long cavity. Figure 15 illustrates what happens to the ion current density as a result of modifying the electron emission temperature boundary condition. For Figs. 14 and 15, electron emission temperature was set at 10 keV and was included to model electron emission from a non-uniform or unstable plasma. However, the 10 keV temperature spreads out the electron and ion densities further off the axis to higher radial values with increased cavity length. This is shown in Fig. 15 by the high $2\pi R J_i$ feature in red stretching from $R = 0.5$–3 cm for the length of the cavity. Thus, we see the orange peaks of the linear ion current density at the back of the cavity in Fig. 14 near $R = 3$ cm.

The same 10-cm-long cavity simulation was performed except that the electron emission temperature was set to 0 keV. In this case, high linear electron and ion densities remain closer to the axis for the
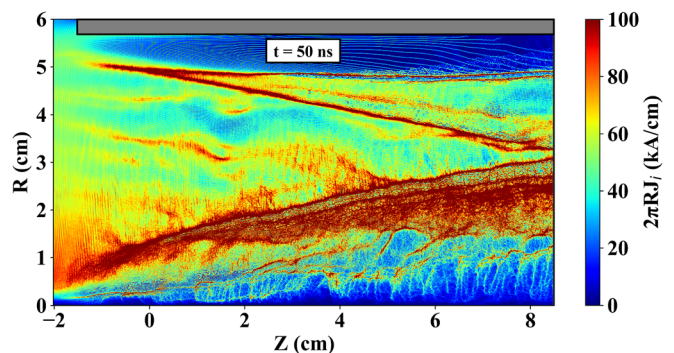

FIG. 15. Linear ion current density at 50 ns for a 10 cm long cavity diode. Electron emission temperature is 10 keV.
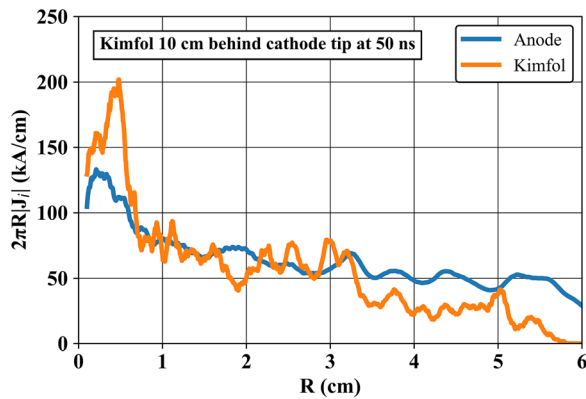
FIG. 16. Linear ion current density 2 mm off anode (blue) and Kimfol (orange) surface for a 10-cm-long cavity simulation. Electron emission temperature is 0 keV.

length of the cavity. Figure 16 is a lineout of the linear ion current density at a point 2 mm off the anode and the back surface of the cavity. In Fig. 16, the linear ion current density is noticeably higher for $R < 1$ cm at both anode and Kimfol surfaces. This is due to beam pinching and the resulting high particle densities near the axis. Thus, increasing electron emission temperature shifts this peak to higher radial locations, which modifies the linear ion current density seen at the back of the cavity in Fig. 14.

Additionally, the effects of hot spots on the linear ion current density are reduced in Fig. 16 as compared to smaller cavities (Fig. 6). This is observed in the small amplitude peaks seen for $R > 1$ cm. This result shows that hot spot effects wash-out and that uniformity is improved between the anode and Kimfol for longer cavities. However, additional investigation is required due to differences observed in the linear ion current density by modifying the electron emission temperature. Future work involves modeling and simulating plasma dynamics or determining an appropriate electron emission temperature that closely matches experimental observation.

V. ION BENDING ANGLES

In addition to the linear ion current density, ion bending angles are of interest. Bending angles are calculated by using the average of individual ion bending angles within 25-μm squares. The bending angle for each ion is computed using Eq. (2) where p_r and p_z are radial and axial momentum components. The average bending angle, $\bar{\theta}$, is obtained using Eq. (3) where W is a sum of ion weights and the subscript i represents individual ions. Positive values indicate inward bending toward the axis and negative values indicate outward bending toward the diode wall

$$\theta_i = -\arctan\left(\frac{p_r}{p_z}\right), \tag{2}$$

$$\bar{\theta} = \frac{1}{W}\sum_{i=1}^{n} w_i \theta_i. \tag{3}$$

Figure 17 shows contour plots of ion bending angles for all cases at 45 ns. The magenta lines on the contour plots represent ion trajectories starting at 40 ns. These trajectories take ~1–2 ns time to
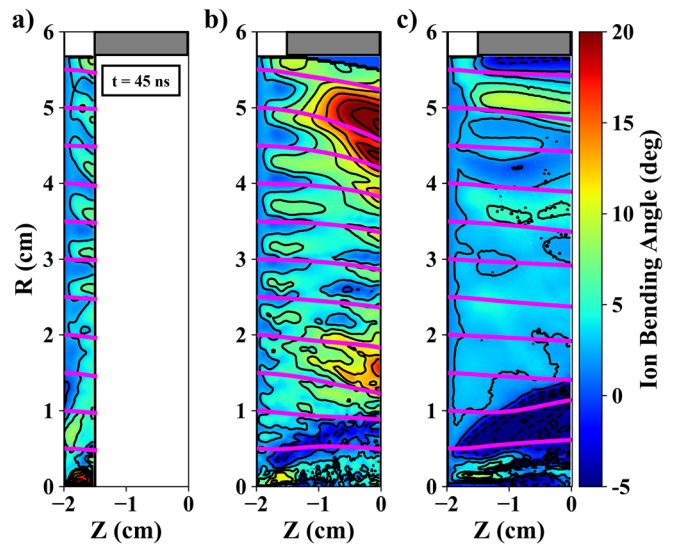

FIG. 17. Ion bending angle contours at t = 45 ns. Magenta lines are ion trajectories that begin at t = 40 ns. (a) Kimfol is flush to the cathode tip. (b) Kimfol is 1.5 cm behind cathode tip. (c) Kimfol is 10 cm behind cathode tip.

completely cross a 2 cm axial length of the simulation region. They are spaced 0.5 cm apart between $R = 0.5$ and 5.5 cm.

A lineout of the bending angles 2 mm off the anode surface is shown in Fig. 18. The bending angles for all cases at that location is small with values between 0° and 5° except for $R < 1$ cm. These small bending angles observed in Fig. 18 are a result of the small radial electric field in the layer between the anode and the virtual cathode discussed above in Sec. II. However, within a distance of 2 mm off the anode surface, hot spot effects also affect the bending angles as seen by the periodic peaks along the radius for Kimfol mounted flush and 1.5 cm behind the cathode tip. Hot spot effects on the bending angles are much less for the 10-cm-long cavity case shown as the green line in Fig. 18.
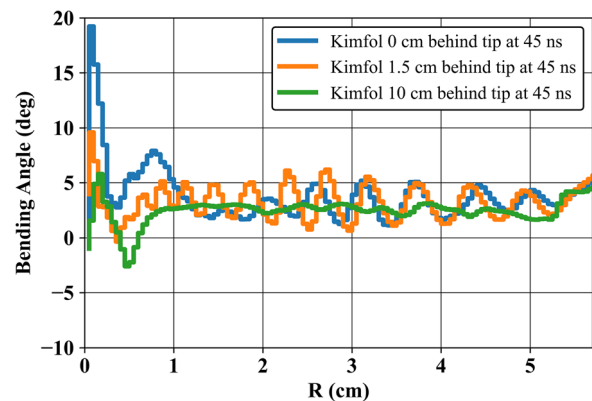

FIG. 18. Ion bending 2 mm off anode surface for: (1) Kimfol flush to the cathode tip (blue), (2) Kimfol 1.5 cm behind cathode tip (orange), and (3) Kimfol 10 cm behind cathode tip (green).

After being emitted from the anode surface, any change in bending angle once the ions reach the Kimfol surface is due to the combination of the radial electric field in the diode region and bending in the magnetic field that arises from the net current behind the cathode tip. Note that these results agree well with experimental observation.[11] However, previous models of estimating ion bending angles did not include any electric field bending between the anode foil and the virtual cathode but overstated the magnetic bending by assuming the ion current rather than the net current beyond the virtual cathode. Regardless, the results between these simulations and previous experiments both predict very similar bending angles.

The flush-mounted Kimfol case shows little difference for ion bending angles between the anode and Kimfol due to the short distance between those surfaces. The fields within this diode have very little time to cause significant bending before ions reach the Kimfol surface. This result is consistent with Fig. 19, which is a lineout of the bending angles near the Kimfol surface for all scenarios.

The 10-cm case (green line) shows smaller magnitudes in bending angles as compared to the other cases. However, outward (negative) bending angles are observed in Fig. 19. This is attributed to the addition of 10 keV temperature to emission electrons in the simulation, which spreads out high particle densities off the axis to higher radial locations. The same analysis on a simulation with 0 keV temperature (not shown) shows high particle densities closer to the axis, which results in small ($<5°$) positive inward bending.

The most noticeable result from all simulation scenarios is that significant bending is observed for Kimfol placed 1.5 cm behind the cathode tip. Figures 17 and 19 show ion bending reaching 15° at approximately $R = 1.5$ cm and greater than 20° between $R = 4$ and 5 cm close to the Kimfol surface. In order to explain this result, an analysis of current flow by particle species is required.

Figure 20 is the cumulative current enclosed ($2\pi\int J_z r \cdot dr$) halfway between the anode and Kimfol for the total and various individual particle species at 45 ns. Figure 20(a) is the case where the Kimfol is located 1.5 cm behind the tip. Figure 20(b) is the case where the Kimfol is located 10 cm behind the tip. The slope of each line indicates the direction of current flow for each species. A positive slope for the ions and a negative slope for the electrons indicate current flows
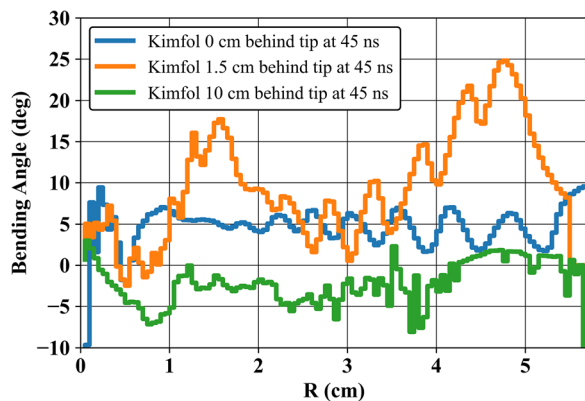

FIG. 19. Ion bending angles 0.5 mm off Kimfol surface for: (1) Kimfol flush to the cathode tip (blue), (2) Kimfol 1.5 cm behind cathode tip (orange), and (3) Kimfol 10 cm behind cathode tip (green).
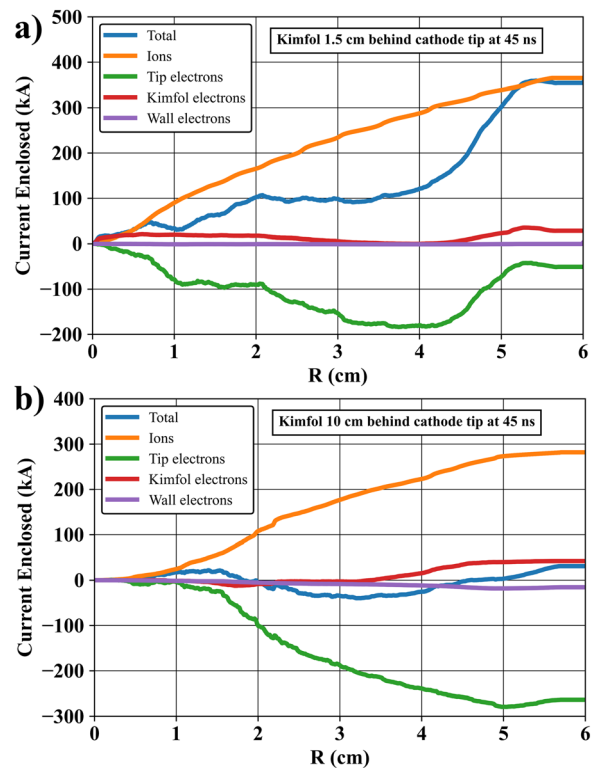

FIG. 20. Current enclosed lineout at 45 ns at a location halfway between anode and Kimfol surfaces. (a) Kimfol placed 1.5 cm behind cathode tip. (b) Kimfol placed 10 cm behind cathode tip.

toward the Kimfol located at the back of the cavity. A positive slope for the electrons indicates that electrons are flowing toward the anode. Regions where the slope is large indicate relatively high current density and regions where it is small indicate small current density.

Defining the species in Fig. 20 is necessary. Tip electrons (green) are defined as electrons that are emitted from the cathode tip surface, which encompasses 0.5 cm behind the cathode tip face. The wall electrons (purple) are emitted from the inner and outer radius of the cathode tip starting at 0.5 cm behind the cathode tip and extend to the surface of the Kimfol. Kimfol electrons (red) are electrons emitted from the Kimfol surface. Overall, Fig. 20 shows that the majority of electron current in the cavity behind the cathode tip comes directly from electrons emitted from the tip. Relatively little current comes from the wall or from the Kimfol at the back surface of the cavity. These results show that electrons are pulled from the pinched electron flow as ions leave the AK gap region and enter the cavity.

For the case where the Kimfol is 1.5 cm behind the tip, Fig. 20(a), tip electrons flow toward the Kimfol between $R = 0–1$ cm and also between $R = 2–4$ cm. This is not surprising as tip electrons from the electron pinch cloud neutralize most of the ion beam and flow with the ions toward the Kimfol surface. This can be seen in Fig. 21(a) that shows a lineout of the electron and ion number densities at a location halfway between the anode and Kimfol. Ion and electron peaks match across most of the radius indicating that electrons are providing charge neutralization of the ion beam. However, in Fig. 20(a), most of the tip
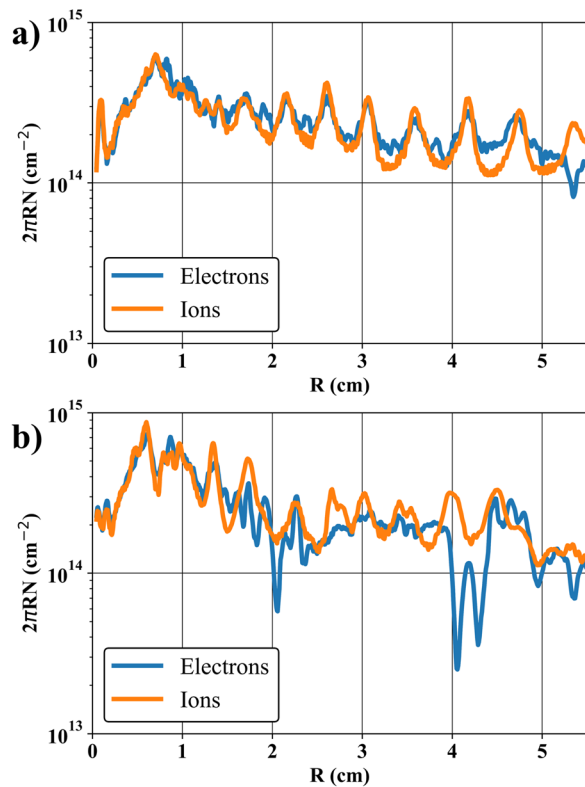
FIG. 21. Linear number density lineouts for Kimfol placed 1.5 cm behind cathode tip. (a) Lineout is halfway between anode and Kimfol. (b) Lineout is 2 mm off Kimfol surface.

electrons return to the AK gap at large radius. It shows that significant tip electron current flows toward the anode between $R = 4$ and 5 cm. This region coincides with a region of high net current and magnetic field [see Fig. 3(a)]. The magnetic field in this region is largely responsible for the large inward bending of the ion orbits seen in Figs. 17 and 19. Figure 21(b) is a lineout of the linear electron and ion number densities 2 mm off the Kimfol surface for Kimfol placed 1.5 cm behind the cathode tip. It shows large charge separation near $R = 2$ and 4 cm. Thus, electron flow toward the anode is caused by an electric field that forms in front of the Kimfol surface late in the pulse.

For Fig. 20(b), tip electrons flow toward the Kimfol across the majority of the radius indicating that electrons are flowing with the ions toward the back of the cavity. The result is consistent with Fig. 8(a), which shows very little net current and magnetic field development behind the tip.

Figure 20(a) also shows that the net current and the total ion current are nearly the same for a 1.5-cm-long cavity. Therefore, a Rogowski coil placed around the cavity would provide an accurate measurement of the ion current in this case.[43] However, Fig. 20(b) shows that the electron and ion current for the 10-cm-long cavity are nearly equal. This causes the net current to be nearly zero across the entire cavity. A Rogowski coil used in the 10-cm-long cavity would not provide a useful estimate of the ion current. Historically, Rogowski coils have been used to measure the ion current with short cavity

lengths of 1 to 2 AK gaps. The measured current for short cavities has also been shown to agree with proton activation estimates of the ion current.[44] For longer cavity lengths, experiments further show that a Rogowski coil drastically underestimates the ion current when compared to proton activation. Our simulation results confirm the experimental rule-of-thumb that Rogowski coils, in conjunction with short cavity lengths, can provide a useful measure of the ion current.[11]

VI. CONCLUSIONS

Particle-in-cell simulations of the ion flow in a pinched electron beam diode show the formation of regions of high electron charge and current density. These hot-spot regions cause the ion-beam current density to be non-uniform as the ions accelerate across the AK gap. Electrons born on the top of the cathode tip experience a strong magnetic field, which causes the electron orbits to be bent away from the anode. Electrons born on the face or bottom of the cathode tip experience a weak magnetic field and are accelerated mostly toward the anode by the strong electric field. When these two streams cross, a hot spot is created that is characterized by a region of locally high charge and current density. As the electrons drift radially inward toward the axis, they experience periodic swings in the electric and magnetic field that produce multiple hot spot regions in the AK gap.

The large electric fields associated with these hot spots modulate the ion-beam current density as it accelerates across the diode AK gap and passes through these electron space-charge hot spots. These hot spots and their effects on the ion current density are more pronounced for the case where the Kimfol is 1.5 cm behind the tip as compared to smaller and larger cavities. For smaller cavities, there are less hot spots because electrons emitted from the Kimfol cause pinch compression against the anode. Additionally, hot spot effects are smaller in amplitude due to the short distance between the anode and Kimfol. Longer cavity lengths increase the number of hot spots but significantly reduce their amplitude, producing a smoother, more uniform ion beam as compared to smaller cavities.

Large bending angles exceeding 20° are observed for a Kimfol placed 1.5 cm behind the cathode tip. These large bending angles are associated with the large net current that develops behind the cathode tip that creates substantial magnetic fields bending ion orbits. The regions of high net current are associated with electrons that flow toward the anode surface. The electron flow toward the anode is caused by an electric field that forms in front of the Kimfol surface late in the pulse. For larger cavities, the ion bending angle is substantially less than the other scenarios. Neutralizing electrons flow with the ions toward the Kimfol across the diode radius. As a result, there is little to no net current or magnetic field that develops behind the tip. Thus, the ion bending angles throughout larger cavities are small.

This work advances understanding of the physics involved with creating more uniform ion beams for materials science-related studies. The results show that larger cavities produce smoother, more uniform ion beams with small bending angles as compared to shorter cavities. However, these results only provide a 2D perspective and future work will expand to 3D in order to provide azimuthal uniformity insight. Future work will also involve modeling electrode plasmas and determining the source of beam micro-divergence. Finally, other diode geometry simulations are planned to further investigate electron hot spot phenomena.

AUTHOR DECLARATIONS

Conflict of Interest

The authors have no conflicts to disclose.

DATA AVAILABILITY

The data that support the findings of this study are available within the article and from the corresponding author upon reasonable request.

REFERENCES

[1] F. Winterberg, Plasma Phys. **17**, 69 (1975).

[2] J. P. VanDevender and D. L. Cook, Science **232**, 831 (1986).

[3] C. L. Olson, J. Fusion Energy **1**, 309 (1981).

[4] S. J. Stephanakis, D. Mosher, G. Cooperstein, J. R. Boller, J. Golden, and S. A. Goldstein, Phys. Rev. Lett. **37**, 1543 (1976).

[5] J. W. Maenchen, F. C. Young, R. Stringfield, S. J. Stephanakis, D. Mosher, S. A. Goldstein, R. D. Genuario, and G. Cooperstein, J. Appl. Phys. **54**, 89 (1983).

[6] A. T. Drobot, R. J. Barker, R. Lee, A. Sternlieb, D. Mosher, and S. A. Goldstein, in *Proceedings of the Third International Topical Conference on High Power Electron and Ion Beam Research and Technology* (Institute of Nuclear Physics, USSR, 1979), p. 647.

[7] A. T. Drobot, A. Palevsky, R. J. Barker, S. A. Goldstein, G. Craig, and D. Mosher, in *Proceedings of the Fourth International Topical Conference on High Power Electron and Ion Beam Research and Technology* (IEEE, 1981), p. 363.

[8] G. Cooperstein, R. J. Barker, J. R. Boller, D. G. Columbant, S. A. Goldstein, R. A. Meger, D. Mosher, W. F. Oliphant, P. F. Ottinger, and A. T. Drobot, *NRL Light Ion Beam Research for Inertial Confinement Fusion* (Plenum Press, New York, 1981), p. 105.

[9] G. Cooperstein, R. J. Barker, D. G. Colombant, A. T. Drobot, S. A. Goldstein, R. A. Meger, D. Mosher, P. F. Ottinger, F. L. Sandel, S. J. Stephanakis, and F. C. Young, *Light-Ion Inertial-Confinement-Fusion Research at NRL* (IAEA, Vienna, 1983), p. 361.

[10] P. F. Ottinger, P. J. Goodrich, D. D. Hinshelwood, D. Mosher, J. M. Neri, D. V. Rose, S. J. Stephanakis, and F. C. Young, Proc. IEEE **80**, 1010 (1992).

[11] J. M. Neri, P. F. Ottinger, D. V. Rose, P. J. Goodrich, D. D. Hinshelwood, D. Mosher, S. J. Stephanakis, and F. C. Young, Phys. Fluids B **5**, 176 (1993).

[12] G. Cooperstein, P. F. Ottinger, S. A. Goldstein, R. J. Barker, D. G. Colombant, R. A. Merger, J. M. Neri, D. Mosher, F. L. Sandel, S. J. Stephanakis, and F. C. Young, "Status of light ion inertial fusion research at NRL," NRL Memorandum Report No. 5219 (Naval Research Laboratory, 1983).

[13] D. J. Johnson, R. J. Leeper, W. A. Stygar, R. S. Coats, T. A. Mehlhorn, J. P. Quintenz, S. A. Slutz, and M. A. Sweeney, J. Appl. Phys. **58**, 12 (1985).

[14] D. J. Johnson, P. L. Dreike, S. A. Slutz, R. J. Leeper, E. J. T. Burns, J. R. Freeman, T. A. Mehlhorn, and J. P. Quintenz, J. Appl. Phys. **54**, 2230 (1983).

[15] R. N. Sudan and D. W. Longcope, Phys. Fluids B **5**, 1614 (1993).

[16] J. W. Maenchen, G. Cooperstein, J. O'Malley, and I. Smith, Proc. IEEE **92**, 1021 (2004).

[17] R. Menon, R. Chandra, A. Roy, K. Joshi, and A. Sharma, IEEE Trans. Plasma Sci. **49**, 1128 (2021).

[18] S. B. Swanekamp, G. Cooperstein, J. W. Schumer, D. Mosher, F. C. Young, P. F. Ottinger, and R. J. Commisso, IEEE Trans. Plasma Sci. **32**, 2004 (2004).

[19] K. Yatsui, X. D. Kang, T. Sonegawa, T. Matsuoka, K. Masugata, Y. Shimotori, T. Satoh, S. Furuuchi, Y. Ohuchi, and T. Takeshita, Phys. Plasmas **1**, 1730 (1994).

[20] W. J. Zhao, G. E. Remnev, S. Yan, M. S. Opekounov, X. Y. Le, V. M. Matvienko, B. X. Han, J. M. Xue, and Y. G. Wang, Rev. Sci. Instrum. **71**, 1045 (2000).

[21] S. A. Goldstein and R. Lee, Phys. Rev. Lett. **35**, 1079 (1975).

[22] S. B. Swanekamp, R. J. Commisso, G. Cooperstein, P. F. Ottinger, and J. W. Schumer, Phys. Plasmas **7**, 5214 (2000).

[23] F. C. Young, J. M. Neri, S. J. Stephanakis, and J. W. Maenchen, Bull. Am. Phys. Soc. **37**, 1562 (1992).

[24] F. C. Young, J. R. Boller, S. J. Stephanakis, T. G. Jones, and J. M. Neri, Rev. Sci. Instrum. **70**, 1201 (1999).

[25] V. K. Tripathi, P. F. Ottinger, and J. Guillory, J. Appl. Phys. **54**, 3043 (1983).

[26] D. D. Hinshelwood, IEEE Trans. Plasma Sci. **11**, 188 (1983).

[27] N. Bruner, D. R. Welch, K. D. Hahn, and B. V. Oliver, Phys. Rev. Spec. Top.—Accel. Beams **14**, 024401 (2011).

[28] D. Goude and J. Threadgold, in *Proceedings of the 2015 Pulsed Power Conference* (IEEE, 2015), pp. 1–6.

[29] See https://www.vosssci.com/products/chicago/chicago.html for "Chicago is a software product of Voss Scientific located in Albuquerque New Mexico" (2021).

[30] D. R. Welch, N. Bennett, T. C. Genoni, D. V. Rose, C. Thoma, C. Miller, and W. A. Stygar, Phys. Rev. Accel. Beams **22**, 070401 (2019).

[31] Kimfol details available from Kimberly-Clark Corporation, Lee, MA 01238, 2022.

[32] P. F. Ottinger, B. V. Weber, D. D. Hinshelwood, J. M. Neri, S. J. Stephanakis, F. C. Young, D. R. Welch, and D. V. Rose, Nucl. Instrum. Methods Phys. Res., Sect. A **464**, 321 (2001).

[33] S. P. Bugaev, E. A. Litvinov, G. A. Mesyats, and D. I. Proskurovskiĭ, Sov. Phys. Usp. **18**, 51 (1975).

[34] P. F. Ottinger, T. J. Renk, and J. W. Schumer, Phys. Plasmas **26**, 023105 (2019).

[35] C. D. Child, Phys. Rev. (Ser. I) **32**, 492 (1911).

[36] I. Langmuir, Phys. Rev. **2**, 450 (1913).

[37] H. R. Jory and A. W. Trivelpiece, J. Appl. Phys. **40**, 3924 (1969).

[38] I. Langmuir and K. B. Blodgett, Phys. Rev. **22**, 347 (1923).

[39] A. E. Blaugrund, G. Cooperstein, and S. A. Goldstein, Phys. Fluids **20**, 1185 (1977).

[40] T. W. L. Sanford, J. A. Halbleib, J. W. Poukey, A. L. Pregenzer, R. C. Pate, C. E. Heath, R. Mock, G. A. Mastin, D. C. Ghiglia, T. J. Roemer, P. W. Spence, and G. A. Proulx, J. Appl. Phys. **66**, 10 (1989).

[41] G. Cooperstein, S. A. Goldstein, D. Mosher, R. J. Barker, J. R. Boller, D. G. Colombant, A. T. Drobot, R. A. Meger, W. F. Oliphant, P. F. Ottinger, F. L. Sandel, S. J. Stephanakis, F. C. Young, J. M. Neri, and R. N. Sudan, *Light-Ion Inertial-Confinement-Fusion Research at NRL* (IAEA, Vienna, 1980), pp. 401–411.

[42] D. D. Hinshelwood, P. F. Ottinger, J. W. Schumer, R. J. Allen, J. P. Apruzese, R. J. Commisso, G. Cooperstein, S. L. Jackson, D. P. Murphy, D. Phipps *et al.*, Phys. Plasmas **18**, 053106 (2011).

[43] W. Rogowski and W. Steinhaus, Arch. Elektrotech. **1**, 141 (1912).

[44] S. J. Stephanakis, private communication (2022).